

pubs.acs.org/NanoLett Letter

# Observation of Ultrastrong Coupling between Substrate and the Magnetic Topological Insulator MnBi<sub>2</sub>Te<sub>4</sub>

Gaomin Li, Xiaohua Wu, Yifan Gao, Xiaoming Ma, Fuchen Hou, Hanyan Cheng, Qiaoling Huang, Yueh-Chun Wu, Matthew C. DeCapua, Yujun Zhang, Junhao Lin, Chang Liu, Li Huang, Yue Zhao,\* Jun Yan,\* and Mingyuan Huang\*



Cite This: Nano Lett. 2022, 22, 3856-3864



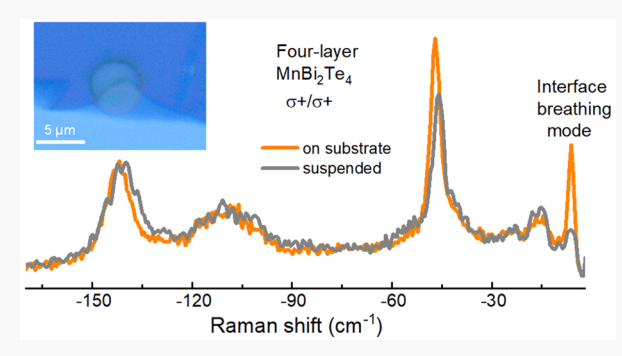
ACCESS

Metrics & More

Article Recommendations

s Supporting Information

ABSTRACT: The intrinsic magnetic topological insulator MnBi<sub>2</sub>Te<sub>4</sub> has attracted significant interest recently as a promising platform for exploring exotic quantum phenomena. Here we report that, when atomically thin MnBi<sub>2</sub>Te<sub>4</sub> is deposited on a substrate such as silicon oxide or gold, there is a very strong mechanical coupling between the atomic layer and the supporting substrate. This is manifested as an intense low-frequency breathing Raman mode that is present even for monolayer MnBi<sub>2</sub>Te<sub>4</sub>. Interestingly, this coupling turns out to be stronger than the interlayer coupling between the MnBi<sub>2</sub>Te<sub>4</sub> atomic layers. We further found that these low-energy breathing modes are highly sensitive to sample degradation, and they become drastically weaker upon ambient air exposure. This is in contrast to the higher



energy optical phonon modes which are much more robust, suggesting that the low-energy Raman modes found here can be an effective indicator of sample quality.

KEYWORDS: MnBi<sub>2</sub>Te<sub>4</sub>, Raman spectroscopy, layer dependence, breathing modes, linear chain model

The quest for interplay between magnetism and topological order has led to the discovery of MnBi<sub>2</sub>Te<sub>4</sub> (MBT), a layered ternary chalcogenide predicted to host versatile nontrivial topological phases.<sup>2-7</sup> An individual MBT layer is seven atoms thick, arranged in the order of Te-Bi-Te-Mn-Te-Bi-Te as illustrated in Figure 1a. Within each septuple layer (SL) of MBT, the Mn ions in the central plane couple to each other ferromagnetically (FM) with an out-ofplane easy axis. Between two neighboring MBT SLs, interlayer exchange interactions between Mn planes are antiferromagnetic (AFM), giving rise to an A-type AFM material system with zero net magnetization at low temperatures.<sup>8–10</sup> Due to a large spin-orbit interaction that causes band inversion and protection from a symmetry composed of time reversal and a half-lattice-constant translation along the c axis, MBT realizes a widely sought after intrinsic magnetic topological insulator. Recent charge transport studies of few-layer MBT indeed showed encouraging signatures of nontrivial topology that are highly sensitive to device layer number. 11-15 Meanwhile, despite the rapid progress, there are several outstanding questions regarding the fundamental properties of MBT. A zero magnetic field quantum anomalous Hall effect is difficult to achieve in MBT thin flakes. Magnetic ordering is anticipated to open a band gap on the top surface of MBT; however, the presence or absence of such a magnetic gap is so far controversial.<sup>3,16–18</sup> Recent studies have revealed that the

surface of MBT is quite sensitive to air exposure and even to trace oxygen/water levels in a controlled environment such as a glovebox, <sup>19</sup> which could cause complications for the even—odd layer dependent nontrivial phases. It is thus of great practical significance to noninvasively and quickly identify the layer number as well as device degradation to understand the fundamental properties of MBT and the possible application of its versatile topological phases and quantum phase transitions.

In this work, we use Raman scattering to study atomic layers of MBT deposited on gold and  $SiO_2/Si$  substrates. A surprisingly strong coupling of MBT flakes to the substrate is observed. This is manifested as an intense breathing mode Raman feature for thin MBT on a substrate that gets significantly suppressed for suspended samples. Our quantitative analysis with a linear chain model shows that the coupling strength between MBT and the substrate is even stronger than the coupling between MBT layers. We further employ Raman scattering to investigate sample degradation under ambient air

Received: October 30, 2021 Revised: April 27, 2022 Published: May 3, 2022





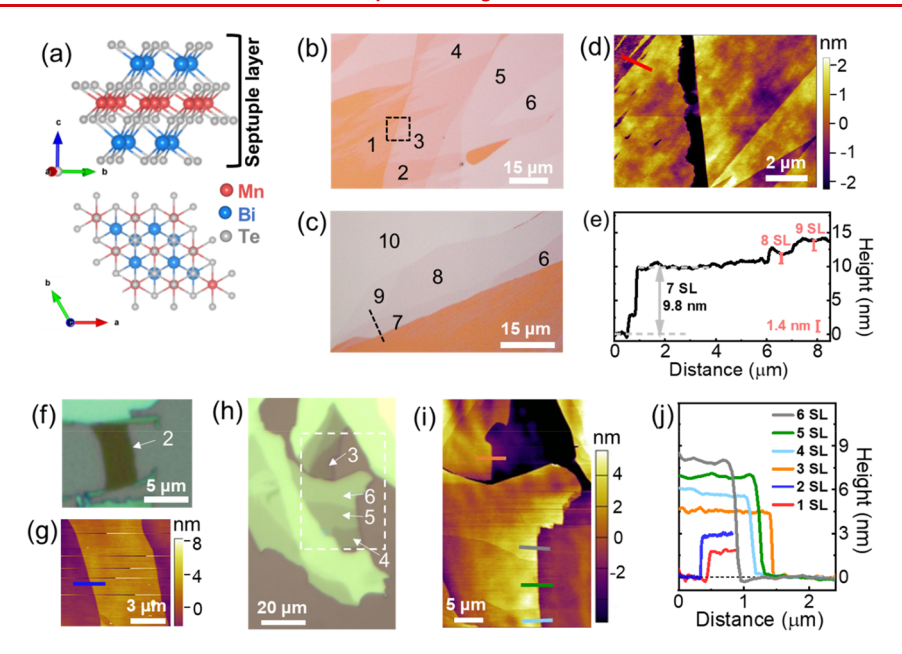


Figure 1. Crystal structure and optical and atomic force microscopy images of MnBi<sub>2</sub>Te<sub>4</sub>. (a) Crystalline structure of MnBi<sub>2</sub>Te<sub>4</sub> (red, Mn; blue, Bi; gray-white, Te), showing the layered structure of MnBi<sub>2</sub>Te<sub>4</sub> along the *c* axis the and triangular structure in the the *ab* plane. The septuple atomic layers are stacked through vdW forces. The lattice vectors of the unit cell are shown as the arrows denoted by **a**, **b**, and **c**. (b, c) Typical optical images of 1–10 SL MnBi<sub>2</sub>Te<sub>4</sub> on a gold substrate. (d) Atomic force microscopy (AFM) micrograph of exfoliated MnBi<sub>2</sub>Te<sub>4</sub> flakes with thicknesses of 1–3 SLs. The height profile of 1 SL on the gold substrate along the red line is shown in (j). (e) Height profiles across the line of 7–9 SLs, denoted with corresponding black dashed line in (c). (f, h) Optical images of 2–6 SL MnBi<sub>2</sub>Te<sub>4</sub> on a SiO<sub>2</sub>/Si substrate. (g, i) AFM micrographs of MnBi<sub>2</sub>Te<sub>4</sub> flakes exfoliated on a SiO<sub>2</sub>/Si substrate: 2 SL and 3–6 SLs in (g) and (i), respectively. (j) Height profiles across the lines of 1–6 SLs, denoted in red, blue, orange, light blue, green and gray in (d), (g), and (i).

exposure. The low-energy breathing modes are highly sensitive, much more so than the higher energy optical phonons which survive over 50 h of ambient air exposure, indicating that the low-wavenumber Raman for the few-layer MBT provides a practical and useful tool to monitor sample degradation.

The high-quality bulk MBT, with 5% Sb doping, is grown using a conventional high-temperature solution method (see Methods). Atomically thin MBT samples down to 1 SL are fabricated from bulk crystals using a mechanical exfoliation method and deposited onto either gold or SiO<sub>2</sub>/Si substrate (details in Methods; additional results on pure MBT, i.e. no Sb doping, are shown in the Supporting Information). Figure 1b,c and Figure 1f,h present typical optical images of MBT flakes on gold and SiO<sub>2</sub>/Si substrates, respectively. These thin samples show different optical contrasts for different layer numbers, and their thicknesses are measured by atomic force microscopy (AFM) in a glovebox (see Figure 1d,g,i). The height line profiles of the 1-SL in Figure 1b, 2-6 SL in Figure 1f,h, and 7-9 SL in Figure 1c are shown in Figure 1e,j. From Figure 1e,j, the step height of each additional MBT SL corresponds to a thickness of about 1.4 nm, which is consistent with previous reports.  $^{20-22}$  The sample with a height of  $\sim 1.7$  nm from the subtract was assigned to 1 SL; this is slightly larger than 1.4 nm, possibly induced by some adsorbates.

We first characterize the vibrational properties of bulk MBT. Figure 2a shows circular (cocircular,  $\sigma^+/\sigma^+$ ; cross-circular,  $\sigma^+/\sigma^-$ ) and linear (parallel, XX; cross, XY) polarization-resolved Raman spectra at room temperature (details are given in Methods). Six intrinsic Raman modes of the bulk samples are observed: three at 46, 109, and 142 cm<sup>-1</sup> in the  $\sigma^+/\sigma^+$  channel, and another three at 27, 68, and 104 cm<sup>-1</sup> in the  $\sigma^+/\sigma^-$  channel, indicating good sample crystallinity. In linearly polarized measurements, all six modes are observable in the

XX channel, and the three modes seen in the  $\sigma^+/\sigma^-$  channel also show up in the XY channel.

At room temperature MBT is paramagnetic. Its unit cell contains only one septuple layer and seven atoms. From a group theory analysis<sup>23</sup> bulk MBT belongs to the point group  $D_{3d}$  (space group R3m), whose character table is shown in Figure 2c. Accordingly, the irreducible representation of MBT atomic displacement for optical phonons at the  $\Gamma$  point is  $\Gamma_{\text{opt}}$ =  $3A_{1g} + 3A_{2u} + 3E_{u} + 3E_{g}$ . Among them, Raman-active modes are  $\Gamma_R = 3A_{1g} + 3E_g$ . The 2-fold degenerate E symmetry modes represent in-plane vibrations, while the nondegenerate A symmetry mode vibrations are out-of-plane vibrations. On the basis of the circular and linear polarization Raman selection rules, the phonon modes at 46, 109, and 143 cm<sup>-1</sup> can be assigned as  $A_{1g}$  modes and 27, 66, and 104 cm<sup>-1</sup> as  $E_g$  modes. This assignment agrees well with our first-principles calculation results given in Figure 2b, as well as previous studies.<sup>23–26</sup> We further determine the eigenvectors of Raman modes with firstprinciples calculations. The atomic displacements of the Raman-active modes are illustrated in Figure 2d,e. The Mn atoms in these modes are stationary, reflecting their even parity nature. These Raman-active vibrations in MBT are somewhat similar to those in materials with similar crystal structures: e.g., Bi<sub>2</sub>Te<sub>3</sub> and Bi<sub>2</sub>Se<sub>3</sub>.<sup>27</sup>

Since circular polarization resolved measurements can exclusively distinguish between in-plane and out-of-plane vibrations (Figure 1a),  $^{28}$  in the following we focus on circular polarization-resolved measurements to study MBT thin films. The circular polarization resolved Raman spectra of MBT on a gold substrate are measured from 11 SL to 1 SL as shown in Figure 3a. We clearly observe the same six optical phonon modes  $3A_{1g} + 3E_{g}$  discussed for the bulk, which display no obvious change from 11 SL to 6 SL. Below 5 SL all of them

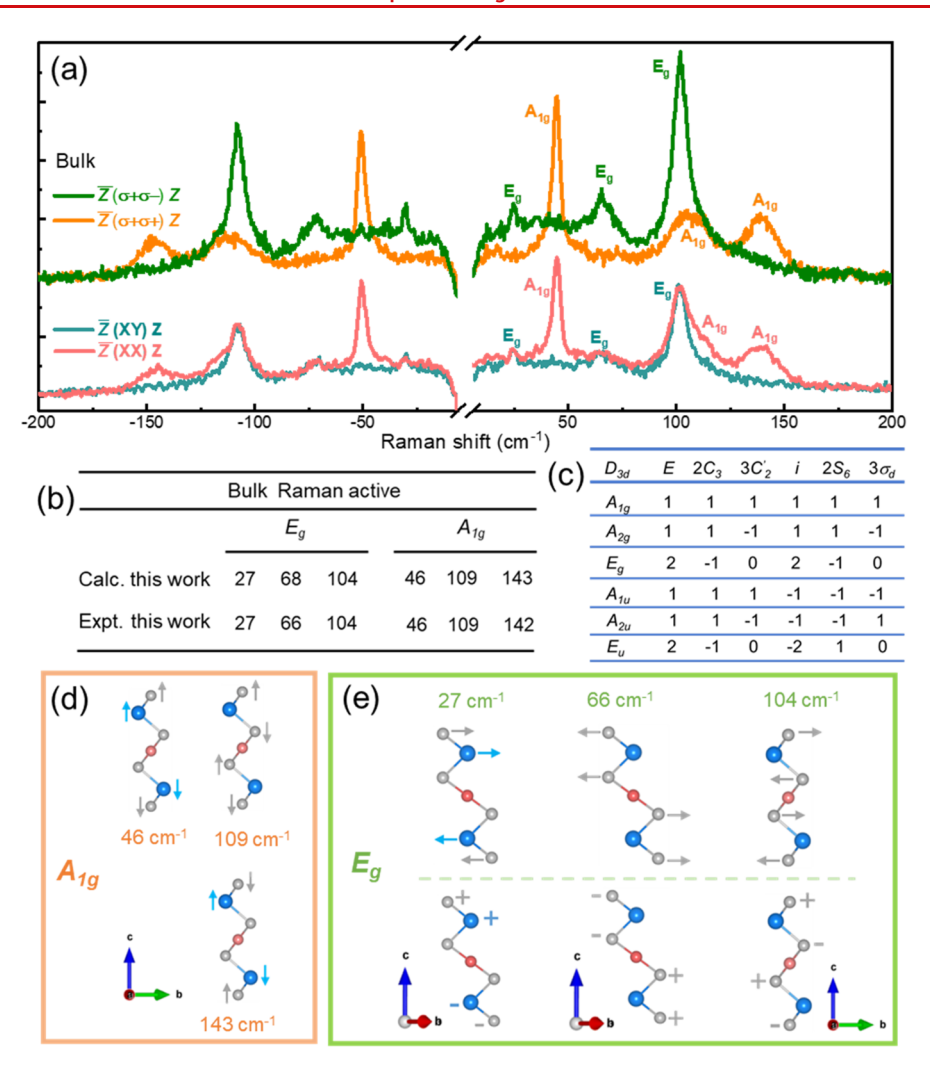


Figure 2. Raman-active vibrational modes of bulk  $MnBi_2Te_4$ . (a) Circularly and linearly polarized Raman spectra of bulk  $MnBi_2Te_4$  at room temperature. (b) Zone-center phonon frequencies (cm<sup>-1</sup>) of  $MnBi_2Te_4$ . (c) Character table of the  $D_{3d}$  point group. (d, e) Displacement schematics of the Raman-active vibrational modes in the bulk sample. The symbols + and - stand for vibrating perpendicularly to the paper, inward and outward, respectively. The long arrows represent the dominant vibrations.

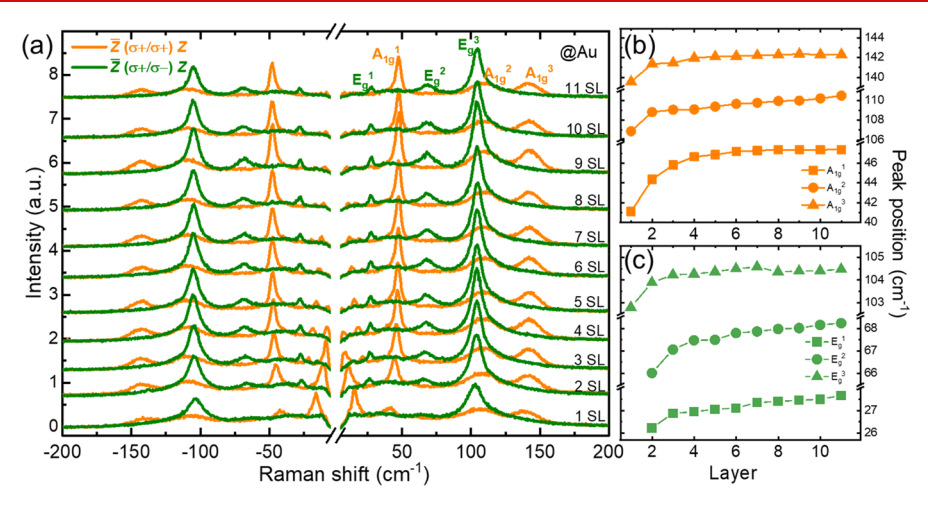


Figure 3. (a) Stokes and anti-Stokes layer dependent Raman spectra of MnBi<sub>2</sub>Te<sub>4</sub> on a gold substrate under  $\overline{Z}(\sigma^+/\sigma^+)Z$  (orange) and  $\overline{Z}(\sigma^+/\sigma^-)Z$  (green) circular polarization configurations in the wavenumber region 6–200 cm<sup>-1</sup>. (b)  $A_{1g}$  mode energy versus thickness. (c)  $E_g$  mode energy versus thickness. The layer-dependent Raman spectra for MBT were taken at room temperature.

experience gradual red shift due to a quantum confinement effect. It is noteworthy that the  $A_{1g}^1$  mode at 46 cm<sup>-1</sup> exhibits

an abrupt intensity decrease from 2 SL to 1 SL and a large red shift of  $\sim\!\!6$  cm<sup>-1</sup> from 11 SL to 1 SL, while the  $A_{1g}^2$  and  $A_{1g}^3$ 

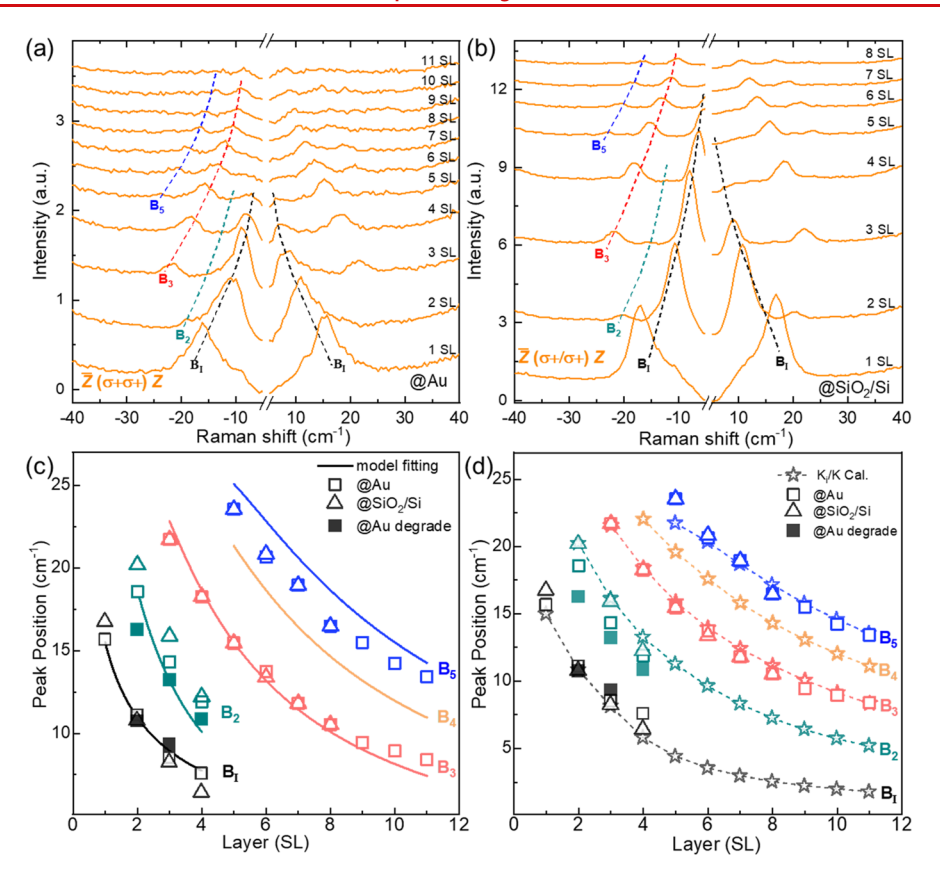


Figure 4. Low-wavenumber Raman spectrum evolution as a function of MnBi<sub>2</sub>Te<sub>4</sub> SL layer number at room temperature. (a, b) Low-wavenumber Raman spectra of MnBi<sub>2</sub>Te<sub>4</sub> thin films on (a) gold and (b) SiO<sub>2</sub>/Si substrates measured using the  $\overline{Z}(\sigma^+/\sigma^+)Z$  circular polarization configuration. (c) Energy evolutions of measured B<sub>1</sub>, B<sub>2</sub>, B<sub>3</sub>, and B<sub>5</sub> modes in MBT on gold (hollow squares, 1–11 SL) and SiO<sub>2</sub>/Si (hollow triangles, 1–8 SL) substrates, as well as the fitting (the solid lines) using the free linear chain model. The solid black and dark green squares are for B<sub>1</sub> and B<sub>2</sub> modes after 2 h degradation, respectively. (d) Comparison between the experimental and the calculated frequencies (star guided by dashed line, 1–11 SL) for the B<sub>1</sub>, B<sub>2</sub>, B<sub>3</sub>, B<sub>4</sub>, and B<sub>5</sub> modes using the linear chain model with  $K_{11}/K = 2$  and  $K_{12}/K = 0.5$  substrate coupling.

peak red shifts are smaller,  $\sim 3~{\rm cm}^{-1}$ . The three  $E_g$  modes show similar red shifts of  $\sim 2~{\rm cm}^{-1}$ . These red shifts may come from the increasing electron—phonon coupling due to the quantum confinement effect in thinner layers. <sup>24,26</sup> We also note that the  $E_g^1$  and  $E_g^2$  modes disappear suddenly for the 1 SL. The reason for this is currently unclear, since from group theory analysis they are expected to be Raman active.

In addition to the six optical phonon modes similar to those in the bulk, additional low-wavenumber Raman modes (<30 cm<sup>-1</sup>) are observed in the thin film samples, attributable to interlayer Raman modes, similarly to other 2D materials. <sup>29–32</sup> These modes appear mostly in the  $\sigma^+/\sigma^+$  channel, suggesting their out-of-plane vibrational nature. Low-energy Raman features (except for the 27 cm<sup>-1</sup> intralayer optical phonon) in the  $\sigma^+/\sigma^-$  channel are weak and hard to identify. In the following we focus on the  $\sigma^+/\sigma^+$  spectra.

Figure 4a shows the layer-dependent low-wavenumber Raman spectra in the  $\sigma^+/\sigma^+$  channel for 1–11 SL MBT on the gold substrate. All of the low-wavenumber Raman modes show significant blue shifts with decreasing layer number and can be classified into four branches we label as  $B_L$ ,  $B_2$ ,  $B_3$ , and  $B_5$ , guided by the black, green, red, and blue dashed lines, respectively, in Figure 4a. Note that  $B_2$  is not as obvious as the other three branches in Figure 4a but can be more clearly identified for the samples deposited on the  $SiO_2/Si$  substrate, as shown in Figure 4b. With an increase in the layer number, the  $B_2$  peak starts to show up from 2 SL, the  $B_3$  peak from 3

SL, and the B<sub>5</sub> peak from 5 SL. These three branches are assigned as interlayer breathing modes. The energies of the breathing modes are very sensitive to the layer number, which makes low-wavenumber Raman spectroscopy a fast and convenient approach for MBT layer number identification. Note that for bulk MBT no low-wavenumber Raman peaks can be observed at all in Figure 2a, which is consistent with the group theory analysis that the interlayer vibrational modes do not exist in bulk MBT, since its unit cell contains only one septuple layer.

Just like the absence of any interlayer Raman modes in the bulk, monolayer MBT is anticipated to have no low-energy breathing or shear modes, as has been demonstrated in other 2D material systems. 28-34 Interestingly in our data, monolayer MBT on a gold substrate displays a strong Raman feature B<sub>I</sub> at about 16 cm<sup>-1</sup>, which shows a layer dependence similar to that of other interlayer breathing modes. We have carefully verified this observation on another substrate of SiO<sub>2</sub>/Si. As shown in Figure 4b, these B<sub>I</sub> modes are at about the same energy on SiO<sub>2</sub>/Si but are more intense and slightly sharper. This makes the B2 modes more visible than those on a gold substrate. For bilayer MBT deposited on SiO<sub>2</sub>/Si, two well-separated breathing modes can be clearly observed. From a general consideration, there should be only one interlayer breathing mode in the bilayer and none in the monolayer. To further investigate the nature of B<sub>D</sub> we fabricated a four-layer sample that is partially suspended over an etched hole on the silicon

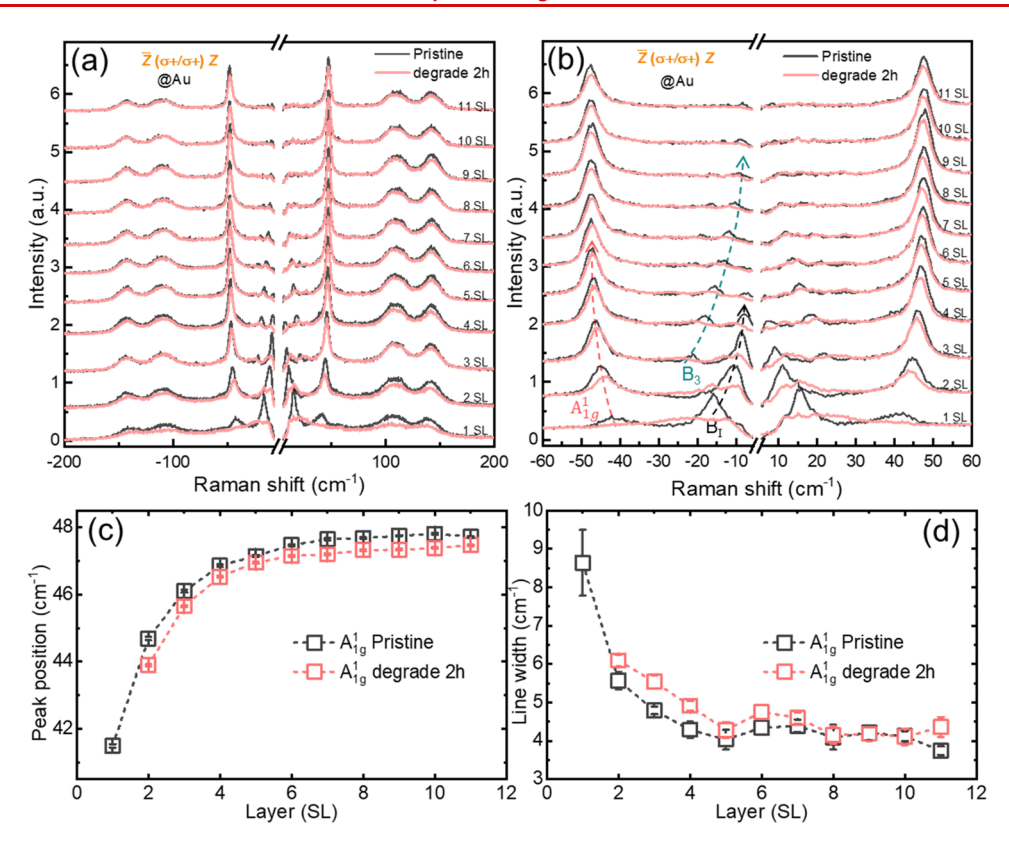


Figure 5. Effect of ambient air exposure on  $MnBi_2Te_4$  thin layers using  $\overline{Z}(\sigma^+/\sigma^+)Z$  circular polarization Raman spectroscopy at room temperature. (a) The 1–11 SL Raman spectra comparison of the "pristine" and "2 h degradation"  $MnBi_2Te_4$  samples on a gold substrate. (b) Enlarged low-wavenumber Raman spectra of 1–11 SL  $MnBi_2Te_4$  thin films on a gold substrate. (c, d) Comparison of peak position (c) and line width (d) for the  $A_{1g}^1$  mode in  $MnBi_2Te_4$  (1–11 SL) on a gold substrate before and after degradation.

substrate. When the laser light is centered on the suspended part, the interface mode  $B_{\rm I}$  is significantly suppressed while other modes are largely the same except for a small red shift, as shown in the table of contents figure. When these results are taken together, the  $B_{\rm I}$  branch is assigned as the interface breathing mode, which originates from the interaction of few-layer MBT with the substrate.

The energies of the observed breathing modes provide a quantitative measurement of the coupling strength between MBT layers as well as between MBT and the substrate. As the simplest estimation, we can assess the interlayer coupling strength using the bilayer  $B_2$  mode energy  $E_{B_2}^{2L}$ . From a measured  $B_2$  value of  $E_{B_2}^{2L} \approx 19 \text{ cm}^{-1}$ , we estimate the MBT interlayer out of plane coupling given by  $K = 2 \mu (\pi c E_{B_2}^{2L})^2 = 6.4 \times 10^{19} \text{ N/m}^3$ , where  $\mu$  is the mass per unit area of one MBT SL ( $\mu = 10.04 \times 10^{-6} \text{ kg/m}^2$ ), c is the speed of light, and K is the force constant per unit area. A more comprehensive analysis employs the linear chain model<sup>29</sup>

$$E_{\mathrm{B}_{\alpha}}^{\mathrm{NL}} = \sqrt{\frac{K}{2\mu\pi^{2}c^{2}} \left(1 - \cos\left(\frac{(\alpha - 1)\pi}{N}\right)\right)} \tag{1}$$

where N denotes the layer number and  $\alpha = 1, 2, ..., N$ . The  $\alpha = 1$  mode corresponds to the acoustic mode and  $\alpha = 2, ..., N$  correspond to the breathing modes  $(K = K_z)$  or shear modes  $(K = K_x)$ . This model can fit the measured frequencies of  $B_2$  and  $B_3$  reasonably well with  $\alpha = 2, 3$  in Figure 4c, and the resulting force constant  $K_z$  is  $6.2 \times 10^{19}$  N/m<sup>3</sup>. For  $B_5$ , neither  $\alpha = 4$  or  $\alpha = 5$  provides an adequate fit, which we will discuss further below. We note that this extracted  $K_z$  value is in

reasonable agreement with the DFT calculation of  $8.21 \times 10^{19}$  N/m³ for Bi<sub>2</sub>Te<sub>3</sub>.<sup>27</sup> This is not surprising, considering the similarity between MBT and Bi<sub>2</sub>Te<sub>3</sub>, especially at the layer interface.

The linear chain model can also be used to extract the MBT-substrate coupling strength

$$E_{\rm B_1}^{\rm NL} = \sqrt{\frac{K_{\rm s}}{4N\mu\pi^2c^2}} \tag{2}$$

where N denotes the layer number,  $\mu$  is the mass per unit area of one MBT SL ( $\mu=10.04\times10^{-6}~{\rm kg/m^2}$ ), c is the speed of light, and  $K_{\rm s}$  is the force constant per unit area between MBT and the substrate out-of-plane coupling. We fit B<sub>I</sub> modes in Figure 4c using eq 2, from which we determine  $K_{\rm s}$  to be  $8.56\times10^{19}~{\rm N/m^3}$  for MBT on a gold substrate. This indicates that the coupling between MBT and the substrate is quite strong, with a strength greater than that between MBT layers.

Considering the very large coupling strength between MBT and the substrate, we incorporate in the linear chain model nonzero substrate introduced force constants  $K_{in}$ , where n denotes the nth MBT layer from the substrate (details are given in the Supporting Information). Figure 4d illustrates such a fit  $K_{i1}/K = 2$ ,  $K_{i2}/K = 0.5$ , and  $K = 4.32 \times 10^{19} \text{ N/m}^3$ . The fit adequately captures the energy evolution of the three interlayer breathing modes  $B_2$ ,  $B_3$ , and  $B_5$ , corresponding to branches of  $\alpha = 2$ , 3, 5, respectively, in contrast to the fits in Figure 4c. We note that with only  $K_{i1}$  we can already achieve reasonable fits. Introducing additional  $K_{in}$  parameters provide better fits to the multilayer  $B_1$  modes. However, the effect of the additional  $K_{in}$  parameters on  $B_2$ ,  $B_3$ , and  $B_5$  mode energies

Nano Letters pubs.acs.org/NanoLett Letter

is small. Figure S1a-c in the Supporting Information illustrates fits with one, two, and three substrate coupling parameters, where we have maintained the same  $K = 4.32 \times 10^{19} \text{ N/m}^3$  in all three fits.

The strong coupling with the substrate also greatly disrupts the symmetry of the phonon modes and, in particular, their Raman activity. In the absence of substrate coupling, the  $\alpha = 2$ , 4 branches of MBT atomic layer breathing modes are Raman active, while  $\alpha = 3$ , 5 branches are Raman inactive. This contradicts our experimental observations, where  $\alpha = 3$  is the most strong MBT breathing mode while the  $\alpha = 2$  branch is much weaker, and one can easily miss it for samples deposited on gold. This observation is quite unusual on comparison with other two-dimensional materials such as transition-metal dichalcogenides, where the  $\alpha = 2$  breathing mode is the strongest, 33 highlighting the prominent effect of substrate coupling. We note that Raman modes due to coupling with the substrate were also observed in Bi<sub>2</sub>Te<sub>3</sub>, <sup>27</sup> albeit there was a less prominent intensity and no breaking of the breathing mode Raman activity was reported.

We now investigate the effect of ambient air exposure on MBT thin layers using Raman spectroscopy. Figure 5a compares two sets of MBT Raman spectra. "Pristine" corresponds to as-made samples, and "degrade 2 h" corresponds to exposure to ambient air for about 2 h. The degradation has a quite dramatic effect on the monolayer: all of its Raman features are greatly broadened and suppressed, and its  $A_{1g}^1$  mode essentially disappeared. For 2+ layers, despite the degradation, the high-energy optical phonons are remarkably robust. We have performed careful tests for extended air exposure up to 50 h (Figure S2 in the Supporting Information); these optical phonon features remain welldefined. There are noticeable changes in the spectra though. As seen from the enlarged comparison in Figure 5b, the  $A_{1g}^1$  peak experiences a slight red shift and line width broadening after degradation. Detailed quantitative analyses are plotted in Figure 5c,d. From Figure 5b, we also observe that the lowwavenumber breathing modes are much more affected by the degradation. In particular, the B<sub>I</sub> and B<sub>3</sub> modes become less intense. Interestingly, this makes  $B_2$  more visible in 2 SL and 3 SL, providing additional support to our assignment of the B<sub>2</sub> branch in Figure 4. The degradation of MBT is currently of great concern in the research community; our Raman results, particularly the low wavenumber modes, provide a sensitive sensor to monitor device degradation.

We systematically investigated and analyzed the phonon modes in thin films of the magnetic topological insulator MnBi<sub>2</sub>Te<sub>4</sub>. The layer-number-dependent Raman mode energies provide a direct method to identify the MBT thickness. We discovered an intense ultralow-wavenumber Raman mode in 1-4 SL MBT on gold and SiO<sub>2</sub>/Si substrates, which is attributed to substrate-MBT interface coupling. Surprisingly, this coupling is stronger than the interlayer coupling between MBT septuple layers. The implications of such a strong substrate coupling on the MBT magnetic and topological properties have been largely unexplored. In particular, surface electronic states are critical for the band topology of MBT thin films and so far theoretical calculations have typically neglected the effect of the substrate. Experimentally conflicting results and interpretations exist regarding the zero quantum anomalous Hall plateau in even and odd layers of MBT, for which the effect of the substrate has not been carefully considered. Finally, we observed the degradation in thin layers

by the change in low-wavenumber Raman modes, suggesting the instability of MBT thin layers in the air. Thus, the layer-dependent Raman study of MBT provides a facile tool to confirm the layer number and monitor sample degradation, which is useful for future quantum phenomena studies.

### METHODS

**Sample Preparation.** High-quality single crystals of MBT with 5% Sb doping were grown by a conventional hightemperature solution method.<sup>35-37</sup> The Mn (purity 99.98%), Bi (99.999%), Sb (99.99%) and Te (99.999%) blocks were weighed and ground in an agate mortar and then placed in an alumina crucible. The alumina crucible was sealed in a quartz tube in an argon environment. The assembly was first heated in a box furnace to 950 °C, held for 10 h, then subsequently cooled to 700 °C over 10 h and further cooled slowly to 575 °C in 100 h. After this heating procedure, the quartz tube was taken out quickly and the contents were then decanted into a centrifuge to remove the excess flux from the single crystals. The thin samples were fabricated by mechanically exfoliating the flakes in a glovebox directly on two different substrates: Au (5 nm)/Cr (3 nm)/SiO<sub>2</sub>/Si (gold) and SiO<sub>2</sub>/Si. For the MnBi<sub>2</sub>Te<sub>4</sub> flakes on SiO<sub>2</sub>/Si, poly(methyl methacrylate) (PMMA) was spin-coated on the sample inside the glovebox right after exfoliaation. After optical measurements, the PMMA was washed away for AFM measurements. All the exfoliation, spin-coating/washing with PMMA, and AFM measurement processes were done inside a glovebox, and these samples were not exposed to air. The MnBi<sub>2</sub>Te<sub>4</sub> flakes on a gold substrate were not protected by PMMA, and there is a brief exposure to the air when the sample is transferred from the glovebox to a cryostat for optical measurements. Crystals without Sb doping were grown and exfoliated similarly. See Figure S3 in the Supporting Information for a comparison of Raman spectra of the two types of samples. The suspended 4 SL MnBi<sub>2</sub>Te<sub>4</sub> sample shown in the table of contents graphic was made using crystals without Sb doping.

Raman Spectroscopy. The circular polarization resolved Raman measurements were performed with a micro-Raman spectrometer (Horiba iHR550) equipped with a liquidnitrogen-cooled CCD detector. The excitation laser (632.8 nm) was first guided through a vertical linear polarizer followed by a quarter-wave plate to achieve  $\sigma^+$  circular polarization. The circular polarization of the excitation light was confirmed at the sample position. All Raman measurements were conducted in the backscattering configuration. The backscattered Raman signal going through the same quarterwave plate was collected and analyzed with a half-wave plate and a linear polarizer. Rotation of the half-wave plate at different angles enabled us to obtain detailed information on the helicity of the scattered light. The scattered light passed through two ultranarrow band notch filters to suppress the Rayleigh scattering light, which enables low-wavenumber measurements down to 5 cm<sup>-1</sup>. The laser power was kept below 0.5 mW. The layer-dependent Raman spectra for MBT were obtained at room temperature. For optical measurements, we took the sample out of the glovebox, quickly put it into the vacuum chamber, and kept it in the vacuum chamber at 10<sup>-6</sup> Torr. When the degradation effects were studied, the sample was exposed to the air before each measurement. In the text, "ambient air" refers to room-temperature, unfiltered air. The humidity in the laboratory was around 60%.

Nano Letters pubs.acs.org/NanoLett Letter

**DFT Calculations.** First-principles calculations were performed within the density functional theory framework using the projected augmented-wave (PAW) method<sup>38</sup> as implemented in the Vienna ab initio simulation package (VASP).<sup>39,40</sup> The exchange-correlation term was treated in the generalized gradient approximation (GGA) of Perdew-Burke-Ernzerhof (PBE). The Kohn-Sham orbitals were expanded in a plane wave basis set with an energy cutoff of 450 eV. All of the structures were optimized until the Hellman-Feynman forces on each atom were smaller than 0.001 eV/Å (10<sup>-5</sup> eV/Å for phonon calculations), and the energy convergence was considered reached when the energy difference was below 10<sup>-7</sup> eV between two consecutive selfconsistent steps. Spin-polarized GGA+U calculations were performed with a  $U_{\rm eff}$  value of 5 eV for Mn atoms, since DFT often provides an unsatisfactory description for such a strongly correlated transition-metal system with localized d orbitals. A 15 × 15 × 15 Γ-centered k-point mesh was used for the kpoint sampling and Brillouin zone integration. Partial occupancies were handled using Gaussian smearing with a broadening width of 0.05 eV. van der Waals corrections were considered using the DFT-D3 method. 42 The phonon modes and frequencies were determined by the frozen phonon method as implemented in the PHONOPY $^{43}$  code at the  $\Gamma$ point.

#### ASSOCIATED CONTENT

## **3** Supporting Information

The Supporting Information is available free of charge at https://pubs.acs.org/doi/10.1021/acs.nanolett.1c04194.

Detailed description of the linear chain model fitting, Raman spectra of samples degraded up to 50 h, Raman spectra of samples without Sb doping, and RMCD of MnBi<sub>2</sub>Te<sub>4</sub> atomic layers (PDF)

## AUTHOR INFORMATION

### **Corresponding Authors**

Yue Zhao — Department of Physics, Southern University of Science and Technology, Shenzhen, Guangdong 518055, People's Republic of China; Shenzhen Institute for Quantum Science and Engineering, Southern University of Science and Technology, Shenzhen 518055, People's Republic of China; orcid.org/0000-0002-9174-0519; Email: zhaoy@sustech.edu.cn

Jun Yan — Department of Physics, University of Massachusetts Amherst, Amherst, Massachusetts 01003, United States; Present Address: On sabbatical at the Department of Physics, Southern University of Science and Technology, Shenzhen 518055, People's Republic of China; orcid.org/0000-0003-3861-4633; Email: yan@physics.umass.edu

Mingyuan Huang — Department of Physics, Southern University of Science and Technology, Shenzhen, Guangdong 518055, People's Republic of China; Email: huangmy@ sustech.edu.cn

## **Authors**

Gaomin Li – Department of Physics, Southern University of Science and Technology, Shenzhen, Guangdong 518055, People's Republic of China; Department of Physics, University of Massachusetts Amherst, Amherst, Massachusetts 01003, United States

- Xiaohua Wu Department of Physics, Southern University of Science and Technology, Shenzhen, Guangdong 518055, People's Republic of China
- Yifan Gao Department of Physics, Southern University of Science and Technology, Shenzhen, Guangdong 518055, People's Republic of China
- Xiaoming Ma Shenzhen Institute for Quantum Science and Engineering, Southern University of Science and Technology, Shenzhen 518055, People's Republic of China
- Fuchen Hou Department of Physics, Southern University of Science and Technology, Shenzhen, Guangdong 518055, People's Republic of China
- Hanyan Cheng Department of Physics, Southern University of Science and Technology, Shenzhen, Guangdong 518055, People's Republic of China
- Qiaoling Huang Department of Physics, Southern University of Science and Technology, Shenzhen, Guangdong 518055, People's Republic of China
- Yueh-Chun Wu Department of Physics, University of Massachusetts Amherst, Amherst, Massachusetts 01003, United States
- Matthew C. DeCapua Department of Physics, University of Massachusetts Amherst, Amherst, Massachusetts 01003, United States
- Yujun Zhang Department of Physics, Southern University of Science and Technology, Shenzhen, Guangdong 518055, People's Republic of China
- Junhao Lin Department of Physics, Southern University of Science and Technology, Shenzhen, Guangdong 518055, People's Republic of China; orcid.org/0000-0002-2195-2823
- Chang Liu Department of Physics, Southern University of Science and Technology, Shenzhen, Guangdong 518055, People's Republic of China; Shenzhen Institute for Quantum Science and Engineering, Southern University of Science and Technology, Shenzhen 518055, People's Republic of China
- Li Huang Department of Physics, Southern University of Science and Technology, Shenzhen, Guangdong 518055, People's Republic of China; orcid.org/0000-0003-0741-4903

Complete contact information is available at: https://pubs.acs.org/10.1021/acs.nanolett.1c04194

#### **Notes**

The authors declare no competing financial interest.

#### ACKNOWLEDGMENTS

M.H. was supported by the National Natural Science Foundation of China (Grant No. 12074165), the Science, Technology and Innovation Commission of Shenzhen Municipality (Grant No. 20200925152344006), and Initiative Funds for Shenzhen High Class University (Grant No. G02206301). J.Y. was supported by the National Science Foundation (DMR-2004474). Y.Z. and X.W. were supported by the National Natural Science Foundation of China under project No. 11674150, the Guangdong Innovative and Entrepreneurial Research Team Program (Grant No. 2016ZT06D348), and the Key-Area Research and Development Program of Guangdong Province (2019B010931001). Y.Z. was supported by the National Natural Science Foundation of China (Grant No. 12104204) and a fellowship

from the China Postdoctoral Science Foundation (Grant No. 2021M691449).

## REFERENCES

- (1) Lee, D. S.; Kim, T. H.; Park, C. H.; Chung, C. Y.; Lim, Y. S.; Seo, W. S.; Park, H. H. Crystal structure, properties and nanostructuring of a new layered chalcogenide semiconductor, Bi<sub>2</sub>MnTe<sub>4</sub>. Cryst. Eng. Comm. 2013, 15, 5532–5538.
- (2) Li, J. H.; Li, Y.; Du, S. Q.; Wang, Z.; Gu, B. L.; Zhang, S. C.; He, K.; Duan, W. H.; Xu, Y. Intrinsic magnetic topological insulators in van der Waals layered MnBi<sub>2</sub>Te<sub>4</sub>-family materials. *Sci. Adv.* **2019**, *5*, No. eaaw5685.
- (3) Otrokov, M. M.; Klimovskikh, I. I.; Bentmann, H.; Estyunin, D.; Zeugner, A.; Aliev, Z. S.; Gass, S.; Wolter, A. U. B.; Koroleva, A. V.; Shikin, A. M.; Blanco-Rey, M.; Hoffmann, M.; Rusinov, I. P.; Vyazovskaya, A. Y.; Eremeev, S. V.; Koroteev, Y. M.; Kuznetsov, V. M.; Freyse, F.; Sanchez-Barriga, J.; Amiraslanov, I. R.; Babanly, M. B.; Mamedov, N. T.; Abdullayev, N. A.; Zverev, V. N.; Alfonsov, A.; Kataev, V.; Buchner, B.; Schwier, E. F.; Kumar, S.; Kimura, A.; Petaccia, L.; Di Santo, G.; Vidal, R. C.; Schatz, S.; Kissner, K.; Unzelmann, M.; Min, C. H.; Moser, S.; Peixoto, T. R. F.; Reinert, F.; Ernst, A.; Echenique, P. M.; Isaeva, A.; Chulkov, E. V. Prediction and observation of an antiferromagnetic topological insulator. *Nature* 2019, 576, 416–422.
- (4) Zhang, D. Q.; Shi, M. J.; Zhu, T. S.; Xing, D. Y.; Zhang, H. J.; Wang, J. Topological Axion States in the Magnetic Insulator MnBi<sub>2</sub>Te<sub>4</sub> with the Quantized Magnetoelectric Effect. *Phys. Rev. Lett.* **2019**, *122*, 206401.
- (5) Tokura, Y.; Yasuda, K.; Tsukazaki, A. Magnetic topological insulators. *Nat. Rev. Phys.* **2019**, *1*, 126–143.
- (6) Gong, Y.; Guo, J. W.; Li, J. H.; Zhu, K. J.; Liao, M. H.; Liu, X. Z.; Zhang, Q. H.; Gu, L.; Tang, L.; Feng, X.; Zhang, D.; Li, W.; Song, C. L.; Wang, L. L.; Yu, P.; Chen, X.; Wang, Y. Y.; Yao, H.; Duan, W. H.; Xu, Y.; Zhang, S. C.; Ma, X. C.; Xue, Q. K.; He, K. Experimental Realization of an Intrinsic Magnetic Topological Insulator. *Chin. Phys. Lett.* 2019, 36, 076801.
- (7) Cui, J. H.; Shi, M. Z.; Wang, H. H.; Yu, F. H.; Wu, T.; Luo, X. G.; Ying, J. J.; Chen, X. H. Transport properties of thin flakes of the antiferromagnetic topological insulator MnBi<sub>2</sub>Te<sub>4</sub>. *Phys. Rev. B: Condens. Matter Mater. Phys.* **2019**, *99*, 155125.
- (8) Otrokov, M. M.; Rusinov, I. P.; Blanco-Rey, M.; Hoffmann, M.; Vyazovskaya, A. Y.; Eremeev, S. V.; Ernst, A.; Echenique, P. M.; Arnau, A.; Chulkov, E. V. Unique Thickness-Dependent Properties of the van der Waals Interlayer Antiferromagnet MnBi<sub>2</sub>Te<sub>4</sub> Films. *Phys. Rev. Lett.* **2019**, *122*, 107202.
- (9) Li, J. H.; Wang, C.; Zhang, Z. T.; Gu, B. L.; Duan, W. H.; Xu, Y. Magnetically controllable topological quantum phase transitions in the antiferromagnetic topological insulator MnBi<sub>2</sub>Te<sub>4</sub>. *Phys. Rev. B: Condens. Matter Mater. Phys.* **2019**, *100*, No. 121103(R).
- (10) Yan, J. Q.; Zhang, Q.; Heitmann, T.; Huang, Z. L.; Chen, K. Y.; Cheng, J. G.; Wu, W. D.; Vaknin, D.; Sales, B. C.; McQueeney, R. J. Crystal growth and magnetic structure of MnBi<sub>2</sub>Te<sub>4</sub>. *Phys. Rev. Mater.* **2019**, *3*, 064202.
- (11) Deng, Y. J.; Yu, Y. J.; Shi, M. Z.; Guo, Z. X.; Xu, Z. H.; Wang, J.; Chen, X. H.; Zhang, Y. B. Quantum anomalous Hall effect in intrinsic magnetic topological insulator MnBi<sub>2</sub>Te<sub>4</sub>. *Science* **2020**, *367*, 895–900.
- (12) Liu, C.; Wang, Y. C.; Li, H.; Wu, Y.; Li, Y. X.; Li, J. H.; He, K.; Xu, Y.; Zhang, J. S.; Wang, Y. Y. Robust axion insulator and Chern insulator phases in a two-dimensional antiferromagnetic topological insulator. *Nat. Mater.* **2020**, *19*, 522–527.
- (13) Ge, J.; Liu, Y. Z.; Li, J. H.; Li, H.; Luo, T. C.; Wu, Y.; Xu, Y.; Wang, J. High-Chern-number and high-temperature quantum Hall effect without Landau levels. *Natl. Sci. Rev.* **2020**, *7*, 1280–1287.
- (14) Zhao, Y. F.; Zhou, L. J.; Wang, F.; Wang, G.; Song, T. C.; Ovchinnikov, D.; Yi, H. M.; Mei, R. B.; Wang, K.; Chan, M. H. W.; Liu, C. X.; Xu, X. D.; Chang, C. Z. Even-Odd Layer-Dependent Anomalous Hall Effect in Topological Magnet MnBi<sub>2</sub>Te<sub>4</sub> Thin Films. *Nano Lett.* **2021**, 21, 7691–7698.

- (15) Ovchinnikov, D.; Huang, X.; Lin, Z.; Fei, Z. Y.; Cai, J. Q.; Song, T. C.; He, M. H.; Jiang, Q. N.; Wang, C.; Li, H.; Wang, Y. Y.; Wu, Y.; Xiao, D.; Chu, J. H.; Yan, J. Q.; Chang, C. Z.; Cui, Y. T.; Xu, X. D. Intertwined Topological and Magnetic Orders in Atomically Thin Chern Insulator MnBi<sub>2</sub>Te<sub>4</sub>. *Nano Lett.* **2021**, *21*, 2544–2550.
- (16) Chen, Y. J.; Xu, L. X.; Li, J. H.; Li, Y. W.; Zhang, C. F.; Li, H.; Wu, Y.; Liang, A. J.; Chen, C.; Jung, S. W.; Cacho, C.; Wang, H. Y.; Mao, Y. H.; Liu, S.; Wang, M. X.; Guo, Y. F.; Xu, Y.; Liu, Z. K.; Yang, L. X.; Chen, Y. L. Topological Electronic Structure and Its Temperature Evolution in Antiferromagnetic Topological Insulator MnBi<sub>2</sub>Te<sub>4</sub>. *Phys. Rev. X* **2019**, *9*, 041040.
- (17) Hao, Y. J.; Liu, P. F.; Feng, Y.; Ma, X. M.; Schwier, E. F.; Arita, M.; Kumar, S.; Hu, C. W.; Lu, R. E.; Zeng, M.; Wang, Y.; Hao, Z. Y.; Sun, H. Y.; Zhang, K.; Mei, J. W.; Ni, N.; Wu, L. S.; Shimada, K.; Chen, C. Y.; Liu, Q. H.; Liu, C. Gapless Surface Dirac Cone in Antiferromagnetic Topological Insulator MnBi<sub>2</sub>Te<sub>4</sub>. *Phys. Rev. X* **2019**, *9*, 041038.
- (18) Yuan, Y.; Wang, X.; Li, H.; Li, J.; Ji, Y.; Hao, Z.; Wu, Y.; He, K.; Wang, Y.; Xu, Y.; et al. Electronic states and magnetic response of MnBi<sub>2</sub>Te<sub>4</sub> by scanning tunneling microscopy and spectroscopy. *Nano Lett.* **2020**, *20*, 3271–3277.
- (19) Hou, F. C.; Yao, Q. S.; Zhou, C. S.; Ma, X. M.; Han, M. J.; Hao, Y. J.; Wu, X. F.; Zhang, Y.; Sun, H. Y.; Liu, C.; Zhao, Y.; Liu, Q. H.; Lin, J. H. Te-Vacancy-Induced Surface Collapse and Reconstruction in Antiferromagnetic Topological Insulator MnBi<sub>2</sub>Te<sub>4</sub>. ACS Nano **2020**, *14*, 11262–11272.
- (20) Li, H.; Liu, S. S.; Liu, C.; Zhang, J. S.; Xu, Y.; Yu, R.; Wu, Y.; Zhang, Y. G.; Fan, S. S. Antiferromagnetic topological insulator MnBi<sub>2</sub>Te<sub>4</sub>: synthesis and magnetic properties. *Phys. Chem. Chem. Phys.* **2020**, 22, 556–563.
- (21) Rienks, E. D. L.; Wimmer, S.; Sanchez-Barriga, J.; Caha, O.; Mandal, P. S.; Ruzicka, J.; Ney, A.; Steiner, H.; Volobuev, V. V.; Groiss, H.; Albu, M.; Kothleitner, G.; Michalicka, J.; Khan, S. A.; Minar, J.; Ebert, H.; Bauer, G.; Freyse, F.; Varykhalov, A.; Rader, O.; Springholz, G. Large magnetic gap at the Dirac point in Bi<sub>2</sub>Te<sub>3</sub>/MnBi<sub>2</sub>Te<sub>4</sub> heterostructures. *Nature* **2019**, *576*, 423–428.
- (22) Yang, S. Q.; Xu, X. L.; Zhu, Y. Z.; Niu, R. R.; Xu, C. Q.; Peng, Y. X.; Cheng, X.; Jia, X. H.; Huang, Y.; Xu, X. F.; Lu, J. M.; Ye, Y. Odd-Even Layer-Number Effect and Layer-Dependent Magnetic Phase Diagrams in MnBi, Te<sub>4</sub>. Phys. Rev. X 2021, 11, 011003.
- (23) Rodriguez-Vega, M.; Leonardo, A.; Fiete, G. A. Group theory study of the vibrational modes and magnetic order in the topological antiferromagnet MnBi<sub>2</sub>Te<sub>4</sub>. *Phys. Rev. B: Condens. Matter Mater. Phys.* **2020**, *102*, 104102.
- (24) Choe, J.; Lujan, D.; Rodriguez-Vega, M.; Ye, Z. P.; Leonardo, A.; Quan, J. M.; Nunley, T. N.; Chang, L. J.; Lee, S. F.; Yan, J. Q.; Fiete, G. A.; He, R.; Li, X. Q. Electron-Phonon and Spin-Lattice Coupling in Atomically Thin Layers of MnBi<sub>2</sub>Te<sub>4</sub>. *Nano Lett.* **2021**, 21, 6139–6145.
- (25) Padmanabhan, H.; Poore, M.; Kim, P.; Koocher, N. Z.; Stoica, V. A.; Puggioni, D.; Wang, H.; Shen, X.; Reid, A. H.; Gu, M. Subpicosecond coherent magnetophononic coupling in MnBi<sub>2</sub>Te<sub>4</sub>. 2021, arXiv:2104.08356 [cond-mat]. arXiv.org e-Print archive. https://arxiv.org/abs/2104.08356 (accessed on Apr 16, 2021).
- (26) Cho, Y.; Kang, J. H.; Liang, L.; Kong, X.; Ghosh, S.; Kargar, F.; Hu, C.; Balandin, A. A.; Puretzky, A. A.; Ni, N. *Phonon modes and Raman signatures of MnBi*<sub>2n</sub>Te<sub>3n+1</sub> (n= 1, 2, 3, 4) magnetic topological heterostructures. 2021, arXiv:2107.03204 [cond-mat]. arXiv.org e-Print archive. https://arxiv.org/abs/2107.03204 (accessed on Jul 26, 2021).
- (27) Zhao, Y. Y.; Luo, X.; Zhang, J.; Wu, J. X.; Bai, X. X.; Wang, M. X.; Jia, J. F.; Peng, H. L.; Liu, Z. F.; Quek, S. Y.; Xiong, Q. H. Interlayer vibrational modes in few-quintuple-layer Bi<sub>2</sub>Te<sub>3</sub> and Bi<sub>2</sub>Se<sub>3</sub> two-dimensional crystals: Raman spectroscopy and first-principles studies. *Phys. Rev. B: Condens. Matter Mater. Phys.* **2014**, *90*, 245428.
- (28) Chen, S. Y.; Zheng, C. X.; Fuhrer, M. S.; Yan, J. Helicity-Resolved Raman Scattering of MoS<sub>2</sub>, MoSe<sub>2</sub>, WS<sub>2</sub>, and WSe<sub>2</sub> Atomic Layers. *Nano Lett.* **2015**, *15*, 2526–2532.
- (29) Liang, L. B.; Zhang, J.; Sumpter, B. G.; Tan, Q. H.; Tan, P. H.; Meunier, V. Low-Frequency Shear and Layer-Breathing Modes in

Nano Letters pubs.acs.org/NanoLett Letter

Raman Scattering of Two-Dimensional Materials. ACS Nano 2017, 11, 11777-11802.

- (30) Zhang, X.; Qiao, X. F.; Shi, W.; Wu, J. B.; Jiang, D. S.; Tan, P. H. Phonon and Raman scattering of two-dimensional transition metal dichalcogenides from monolayer, multilayer to bulk material. *Chem. Soc. Rev.* **2015**, *44*, 2757–2785.
- (31) Li, X. L.; Han, W. P.; Wu, J. B.; Qiao, X. F.; Zhang, J.; Tan, P. H. Layer-Number Dependent Optical Properties of 2D Materials and Their Application for Thickness Determination. *Adv. Funct. Mater.* **2017**, *27*, 1604468.
- (32) Zhao, Y.; Luo, X.; Li, H.; Zhang, J.; Araujo, P. T.; Gan, C. K.; Wu, J.; Zhang, H.; Quek, S. Y.; Dresselhaus, M. S.; et al. Interlayer breathing and shear modes in few-trilayer MoS<sub>2</sub> and WSe<sub>2</sub>. *Nano Lett.* **2013**, *13*, 1007–1015.
- (33) Goldstein, T.; Chen, S. Y.; Tong, J. Y.; Xiao, D.; Ramasubramaniam, A.; Yan, J. Raman scattering and anomalous Stokes-anti-Stokes ratio in MoTe<sub>2</sub> atomic layers. *Sci. Rep.* **2016**, *6*, 1–7
- (34) Chen, S.-Y.; Naylor, C. H.; Goldstein, T.; Johnson, A. C.; Yan, J. Intrinsic phonon bands in high-quality monolayer T' molybdenum ditelluride. *ACS Nano* **2017**, *11*, 814–820.
- (35) Chen, B.; Fei, F. C.; Zhang, D. Q.; Zhang, B.; Liu, W. L.; Zhang, S.; Wang, P. D.; Wei, B. Y.; Zhang, Y.; Zuo, Z. W.; Guo, J. W.; Liu, Q. Q.; Wang, Z. L.; Wu, X. C.; Zong, J. Y.; Xie, X. D.; Chen, W.; Sun, Z.; Wang, S. C.; Zhang, Y.; Zhang, M. H.; Wang, X. F.; Song, F. Q.; Zhang, H. J.; Shen, D. W.; Wang, B. G. Intrinsic magnetic topological insulator phases in the Sb doped MnBi<sub>2</sub>Te<sub>4</sub> bulks and thin flakes. *Nat. Commun.* **2019**, *10*, 4469.
- (36) Aliev, Z. S.; Amiraslanov, I. R.; Nasonova, D. I.; Shevelkov, A. V.; Abdullayev, N. A.; Jahangirli, Z. A.; Orujlu, E. N.; Otrokov, M. M.; Mamedov, N. T.; Babanly, M. B.; Chulkov, E. V. Novel ternary layered manganese bismuth tellurides of the MnTe-Bi<sub>2</sub>Te<sub>3</sub> system: Synthesis and crystal structure. *J. Alloys Compd.* **2019**, 789, 443–450.
- (37) Ma, X.-M.; Zhao, Y.; Zhang, K.; Kumar, S.; Lu, R.; Li, J.; Yao, Q.; Shao, J.; Hou, F.; Wu, X. Realization of a tunable surface Dirac gap in Sb-doped MnBi<sub>2</sub>Te<sub>4</sub>. *Phys. Rev. B: Condens. Matter Mater. Phys.* **2021**, *103*, L121112.
- (38) Blochl, P. E. Projector augmented-wave method. *Phys. Rev. B: Condens. Matter Mater. Phys.* **1994**, *50*, 17953–17979.
- (39) Kresse, G.; Furthmüller, J. Efficiency of ab-initio total energy calculations for metals and semiconductors using a plane-wave basis set. *Comput. Mater. Sci.* **1996**, *6*, 15–50.
- (40) Kresse, G.; Furthmüller, J. Efficient iterative schemes for ab initio total-energy calculations using a plane-wave basis set. *Phys. Rev. B: Condens. Matter Mater. Phys.* **1996**, *54*, 11169.
- (41) Perdew, J. P.; Burke, K.; Ernzerhof, M. Generalized gradient approximation made simple. *Phys. Rev. Lett.* **1996**, *77*, 3865.
- (42) Grimme, S.; Antony, J.; Ehrlich, S.; Krieg, H. A consistent and accurate ab initio parametrization of density functional dispersion correction (DFT-D) for the 94 elements H-Pu. *J. Chem. Phys.* **2010**, 132, 154104.
- (43) Togo, A.; Tanaka, I. First principles phonon calculations in materials science. *Scripta Mater.* **2015**, *108*, 1–5.

## **□** Recommended by ACS

Electronic States and Magnetic Response of MnBi2Te4 by Scanning Tunneling Microscopy and Spectroscopy

Yonghao Yuan, Qi-Kun Xue, et al.

APRIL 16, 2020 NANO LETTERS

READ 🗹

Tunable Magnetic Transition to a Singlet Ground State in a 2D van der Waals Layered Trimerized Kagomé Magnet

Christopher M. Pasco, Tyrel M. McQueen, et al.

JULY 16, 2019

ACS NANO

READ

Giant Topological Hall Effect in the Noncollinear Phase of Two-Dimensional Antiferromagnetic Topological Insulator MnBi4Te7

Subhajit Roychowdhury, Claudia Felser, et al.

OCTOBER 19, 2021

CHEMISTRY OF MATERIALS

READ **C** 

Compositional Control and Optimization of Molecular Beam Epitaxial Growth of (Sb2Te3)1-x(MnSb2Te4)x Magnetic Topological Insulators

Ido Levy, Maria C. Tamargo, et al.

MARCH 31, 2022

CRYSTAL GROWTH & DESIGN

READ 🗹

Get More Suggestions >